Applied Physics Letters ARTICLE pubs.aip.org/aip/apl

Toward dopant-free transparent electronics: Cu_3SiS_4 as a stable intrinsic *p*-type conductor

Cite as: Appl. Phys. Lett. **128**, 142104 (2026); doi: 10.1063/5.0318074
Submitted: 19 December 2025 · Accepted: 16 March 2026 ·
Published Online: 6 April 2026

View Online

Export Citation

CrossMark

Changqing Lin,[1,2] Yu-Jun Zhao,[3] Clas Persson,[4] and Dan Huang[1,2,a)]

AFFILIATIONS

[1]School of Physical Science and Technology, Guangxi University, Nanning 530004, China
[2]Guangxi Key Laboratory of Precision Navigation Technology and Application, Guilin 541004, China
[3]Department of Physics, South China University of Technology, Guangzhou 510640, China
[4]Department of Materials Science and Engineering, KTH Royal Institute of Technology, SE-100 44 Stockholm, Sweden

[a)]Author to whom correspondence should be addressed: danhuang@gxu.edu.cn

ABSTRACT

Traditional transparent conductive materials rely on extrinsic doping of wide bandgap semiconductors, a route that faces thermodynamic limits for *p*-type systems. Here, an inverse strategy is adopted: start with an intrinsically high hole density sulfide and engineer its bandgap for optical transparency. By isovalent Sn → Si substitution in the *p*-type semiconductor Cu_3SnS_4, we obtain orthorhombic Cu_3SiS_4. First-principles calculations find the Fermi level 0.65 eV below the valence band maximum while retaining a wide 2.94 eV fundamental gap, so 40 nm thin films transmit 80% of visible light. Thermodynamic and kinetic stability analyses confirm its chemical stability, indicating that Cu_3SiS_4 should be a highly promising candidate for high-performance intrinsic *p*-type transparent conductive materials.

Published under an exclusive license by AIP Publishing. https://doi.org/10.1063/5.0318074

05 April 2026 16:11:57

Transparent conductive materials (TCMs), as the core functional layer of optoelectronic devices, play an indispensable role in fields such as display technology, photovoltaic devices, and sensors.[1,2] Ideal TCMs should simultaneously possess high light transmittance (typically > 80%) in the visible light range and low resistivity ($<10^{-4}\,\Omega$ cm), meeting the seemingly contradictory properties of optical transparency and excellent electrical conductivity.[3,4] According to the type of majority carriers, TCMs are mainly classified into *p*-type and *n*-type. Currently, most high-performance TCMs are *n*-type, such as Sn-doped In_2O_3 (ITO),[5] Al-doped ZnO (AZO),[6] and F-doped SnO_2 (FTO).[7] As an example, ITO exhibits an electrical conductivity of up to $\sim 10^4$ S cm^{-1} while maintaining a transmittance of approximately 80% in the visible light range. Therefore, the compound is widely used in modern display devices such as liquid crystal displays and touch screens.[8–11] By contrast, the performance parameters of *p*-type TCMs are significantly inferior to those of *n*-type counterparts. Existing studies have shown that the highest-performance *p*-type TCM is Mg- and N-codoped $CuCrO_2$, with a *p*-type electrical conductivity of 278 S cm^{-1} and a visible light transmittance of 69%.[12] The performance gap between *p*-type and *n*-type TCMs has greatly restricted the construction of full-TCM-based electronic devices. If high-performance *p*-type and *n*-type TCMs can be synchronously developed and then transparent p–n junctions can be constructed, it is expected to be used for fabricating transparent transistors, thereby advancing the era of transparent electronic devices. Therefore, high-performance p-TCMs have become one of the key technical bottlenecks in the current field of transparent optoelectronics.

Traditionally, TCMs are engineered by introducing defects into wide bandgap (E_g) semiconductors that remain transparent in the visible range. However, the intrinsic limitations of defect physics hinder the achievement of high carrier concentrations. These constraints make it challenging to identify host materials that offer both a wide E_g and strong doping tolerance, while at the same time avoiding carrier compensation and structural distortion.[13–15] To address the issues, Zunger *et al.* proposed an innovative design concept in the field of TCMs in 2015.[16] By reconstructing the underlying physical design principles of TCMs, they put forward the concept of "intrinsic transparent conductors (ITCs)," which provides a new approach for breaking the bottleneck in this field. In contrast to conventional approaches, this design strategy starts with opaque conductors featuring intrinsically high carrier concentrations, and then imparts optical transparency to these materials via band structure engineering—thus realizing the characteristic of "intrinsic transparent conductivity" in a dopant-free manner. For ITCs, two key conditions must be satisfied: first, in their electronic structure, a sufficiently wide "transparent window" (E_g^{tra}) must exist below (for *n*-type materials) or above (for *p*-type

Published under an exclusive license by AIP Publishing

materials) the Fermi level (E_F) to ensure that interband transitions within this window do not significantly absorb visible light; second, the plasmon frequency (ω_p) of the material must be sufficiently low (e.g., much lower than that of metal Al, $\sim$15 eV/$\hbar$) to suppress the light reflection effect caused by free carriers. In this way, the material can effectively guarantee optical transparency while maintaining a high carrier concentration. Based on this approach, Zunger *et al.* predicted the *n*-type ITC $Ag_3Al_{22}O_{34}$, but they have not yet put forward an ideal intrinsic *p*-type counterpart.[17] Subsequently, Wei *et al.* further proposed shifting the research direction of TCM from "semiconductor doping" to "metal-regulated transparency." Through the synergetic effect of manipulating the symmetry and spatially distributed forbidden transitions between energy bands around the E_F, the matrix elements of carrier transitions can be modulated, ultimately achieving optical transparency while retaining the high electrical conductivity (without doping).[18] They took the zero-dimensional electride $K_4Al_3(SiO_4)_3$ as a paradigm to conduct theoretical analysis and performance verification, demonstrating that it possesses both ultraviolet transparency and metallic conductivity. Through isovalent element substitution combined with high-throughput calculations, they screened out 14 potential intrinsic dopant-free TCMs. These materials all exhibit good electrical conductivity, visible light transparency, and stability, but again display only *n*-type conductivity.

As depicted in Fig. 1, the key requirements for the band structure of intrinsic *p*-type TCMs can be derived from the band structure inversion of intrinsic *n*-type systems. Guided by these criteria and the innovative works[17,18] on intrinsic *n*-type TCMs, the exploration of intrinsic *p*-type TCMs should first involve screening suitable intrinsic *p*-type conductors with good stability, and then be followed by targeted optimization of their optical properties; in this process, good *p*-type conductive characteristics can be maintained while enhancing visible light transmittance, thereby obtaining intrinsic *p*-type TCMs with outstanding comprehensive performance. In fact, in relevant papers integrating experimental and theoretical research, some materials have exhibited intrinsic *p*-type conductor characteristics: their experimental test data confirm *p*-type conductive behavior, and first-principles calculations show that the Fermi levels of these materials are located below the valence band maximum (VBM) and within the valence band, indicating that the system has formed a stable hole-dominated conduction mechanism.[19,20] For example, Cu_3SnS_4 is often reported as a degenerate *p*-type semiconductor. Hall effect experimental measurements show that it has a high carrier concentration ($\sim 6 \times 10^{21}$ cm^{-3}) and low resistivity ($3.5–7.4 \times 10^{-4}$ Ω cm).[21,22] First-principles calculations[20] based on hybrid density functional indicate that its E_F is located below the VBM, suggesting a high density of holes in the system. The calculated band structure reveals a direct E_g of about 0.9 eV at the Γ point above the E_F, which is consistent with the absorption onset at roughly 1.0 eV in the optical absorption spectrum. Although Cu_3SnS_4 exhibits excellent *p*-type conductivity, its narrow E_g^{tra} results in significant absorption of photons in the visible light range, making it hard to maintain visible light transparency. Homovalent element substitution is a widely used method for adjusting the band structure of materials.[23,24] To increase the width of the E_g above its E_F, replacement of Sn with Ge and Si (which have smaller atomic radii) is expected to raise the conduction band energy level, increase the E_g width, effectively expand the E_g^{tra}, and thus improve the visible light transparency, as shown in Fig. 1. Currently, there are no experimental reports on Cu_3GeS_4 and Cu_3SiS_4. However, in the crystal structure databases Atomly[25] and OQMD,[26] established by high-throughput calculations, both Cu_3GeS_4 and Cu_3SiS_4 are shown to be thermodynamically stable compounds. Nevertheless, the calculations of these databases are all based on the generalized gradient approximation functional, which usually underestimates the E_g width of materials, making it difficult to accurately judge their visible light transparency.[27]

In this work, we investigate the electronic and optical properties of Cu_3IVS_4 (IV = Si, Ge, and Sn) based on first-principles density

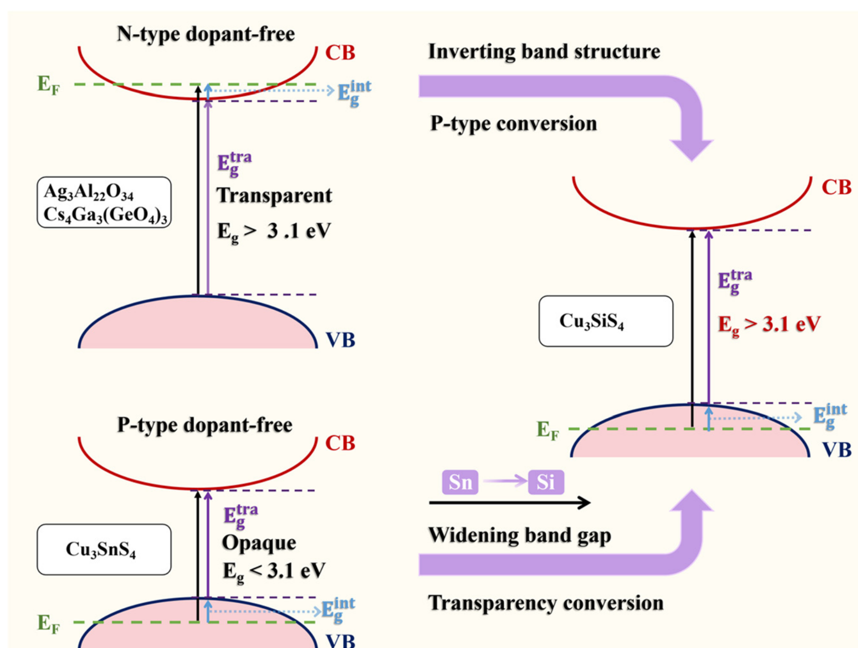

FIG. 1. Schematic for intrinsic *p*-type transparent conductor design.

05 April 2026 16:11:57

Published under an exclusive license by AIP Publishing

functional theory (DFT) calculations using a hybrid functional approach. These compounds all exhibit intrinsic *p*-type conductivity, with their valence band maxima arising from Cu-d and S-p antibonding states. Substituting the group-IV element from Sn to Ge to Si progressively widens the E_g above the Fermi level, thereby expanding the optical transparent window. Notably, Cu_3SiS_4 shows a significantly reduced absorption in the visible range, achieving ∼80% transmittance at 40 nm thickness, while maintaining high *p*-type conductivity. Its thermodynamic and kinetic stability is also confirmed. These results demonstrate the potential of Cu_3SiS_4 as an intrinsic *p*-type transparent conductor and illustrate how compositional tuning can synergistically optimize electronic and optical properties for targeted material design.

As the starting point of our investigation, the parent compound Cu_3SnS_4 has been confirmed by previous experiments[21,22] to possess outstanding *p*-type conductivity. However, its narrow E_g^{tra} restricts its visible light transparency.[18] To address this limitation, we employ the isovalent substitution strategy (replacing Sn with Ge and Si) to regulate the band structure. Since the electronic properties are intrinsically determined by the crystal symmetry, identifying the ground-state structure is the prerequisite for our study. It has been reported that Cu_3SnS_4 can form three crystal structures, namely tetragonal (space group: $I\bar{4}2m$), orthorhombic (space group: $Pmn2_1$), and cubic (space group: $P\bar{4}3m$); see Fig. S1 in the supplementary material. Based on this, the objective of our study is to replace Sn with Ge and Si, aiming to analyze their regulatory mechanism on the band structure, examine the improvement effect of the material's visible light transparency, explore the phase structure stability of the new compounds, and ultimately evaluate their feasibility as intrinsic *p*-type TCMs. According to the calculated total energies of three crystal structures for Cu_3IVS_4 compounds presented in Table I, the tetragonal phase of Cu_3SnS_4 has the lowest energy and is the most stable structure. The energies of the orthorhombic and cubic phases are 10.7 and 8.6 meV/atom higher than that of the tetragonal phase, respectively, which is consistent with the conclusions on phase structure stability reported in previous experiments.[21,22] Similarly, the tetragonal phase is the most stable for Cu_3GeS_4, with the orthorhombic and cubic phases having energies 7.0 and 7.6 meV/atom higher than it, respectively. In contrast, the most stable structure of Cu_3SiS_4 shifts to the orthorhombic phase, and the energies of the tetragonal and cubic phases are 6.7 and 3.8 meV/atom higher than that, respectively. The trend of stable crystal structure types of the aforementioned compounds is consistent with the crystal structures recorded in the Atomly crystal database.[25] The key mechanism underlying this structural difference is that the small ionic radius of Si^{4+} induces significant contraction of its tetrahedral coordination environment, which in turn enhances overall crystal distortion and impairs structural order. Ultimately, the crystal can only relieve internal stress through a distorted structure. In contrast, Ge^{4+} and Sn^{4+} exhibit better radius compatibility with Cu^+, thereby facilitating the formation of high-symmetry crystal structures.[28–30]

Figures S2 and S3 in the supplementary material present the partial density of states (PDOS) and crystal orbital overlap population (COOP) of tetragonal and orthorhombic Cu_3IVS_4, respectively. As can be seen from the figures, the E_F crosses the top of the valence band, exhibiting typical *p*-type conductivity characteristics. The analysis combining PDOS and COOP reveals that the distribution of PDOS and bonding characteristics of the two-phase structures are basically consistent: the top of the valence band is mainly composed of the antibonding states of Cu-d and S-p, while the bottom of the conduction band is dominated by the antibonding states of IV-s and S-p. Figures 2(a)–2(c) and 2(d)–2(f) present the fatband diagrams of tetragonal and orthorhombic Cu_3IVS_4, respectively. The results indicate that the band structures of all systems exhibit *p*-type conductivity characteristics. Specifically, the E_g widths (i.e., E_g^{tra}) above the E_F for tetragonal Cu_3SnS_4, Cu_3GeS_4, and Cu_3SiS_4 are 1.23, 1.87, and 3.00 eV, respectively. With the IV-group element substituted sequentially from Sn to Ge and Si, the conduction band minimum (CBM) shifts toward the higher energy region, and the E_g width gradually increases. This trend can be explained by the variation characteristics of atomic orbital energy levels, bonding modes, and bond strength: the Si–S bond is the shortest with the strongest bonding interaction, while the Sn–S bond is the longest (Table SI). Since the CBM of Cu_3SiS_4 is composed of the anti-bonding states of Si-s and S-p, these anti-bonding states are pushed to a higher energy position, thereby leading to an increase in the E_g width. The E_g widths of orthorhombic Cu_3SnS_4, Cu_3GeS_4, and Cu_3SiS_4 are 1.21, 1.84, and 2.94 eV, respectively, which are slightly smaller than those of their corresponding tetragonal phases. This is mainly attributed to the lower structural symmetry of the orthorhombic phase: the elongation of certain IV–S bond lengths (Table SI in the

TABLE I. Calculated lattice parameters, unit cell volumes [Å^3 per molecular formula (m.f.)], and relative total energies (meV/atom) of Cu_3IVS_4 in three crystal phases. Energies are referenced to those of the tetragonal phase, with boldface denoting the energy value of the most stable crystal phase for each compound.

Compounds	Phases	Lattice parameters			Volume (Å^3/m.f.)	ΔE_{tot} (meV/atom)
		a (Å)	b (Å)	c (Å)		
Cu_3SiS_4	Tetragonal	5.199	5.199	10.470	141.520	0
	Orthorhombic	**7.171**	**6.427**	**6.139**	**141.466**	**−0.67**
	Cubic	5.214	5.214	5.214	141.760	3.8
Cu_3GeS_4	**Tetragonal**	**5.246**	**5.246**	**10.596**	**145.827**	**0**
	Orthorhombic	7.289	6.479	6.190	146.153	7.0
	Cubic	5.266	5.266	5.266	146.071	7.6
Cu_3SnS_4	**Tetragonal**	**5.330**	**5.330**	**10.926**	**155.214**	**0**
	Orthorhombic	7.502	6.572	6.308	155.493	10.7
	Cubic	5.381	5.381	5.381	155.787	8.6

Published under an exclusive license by AIP Publishing
05 April 2026 16:11:57

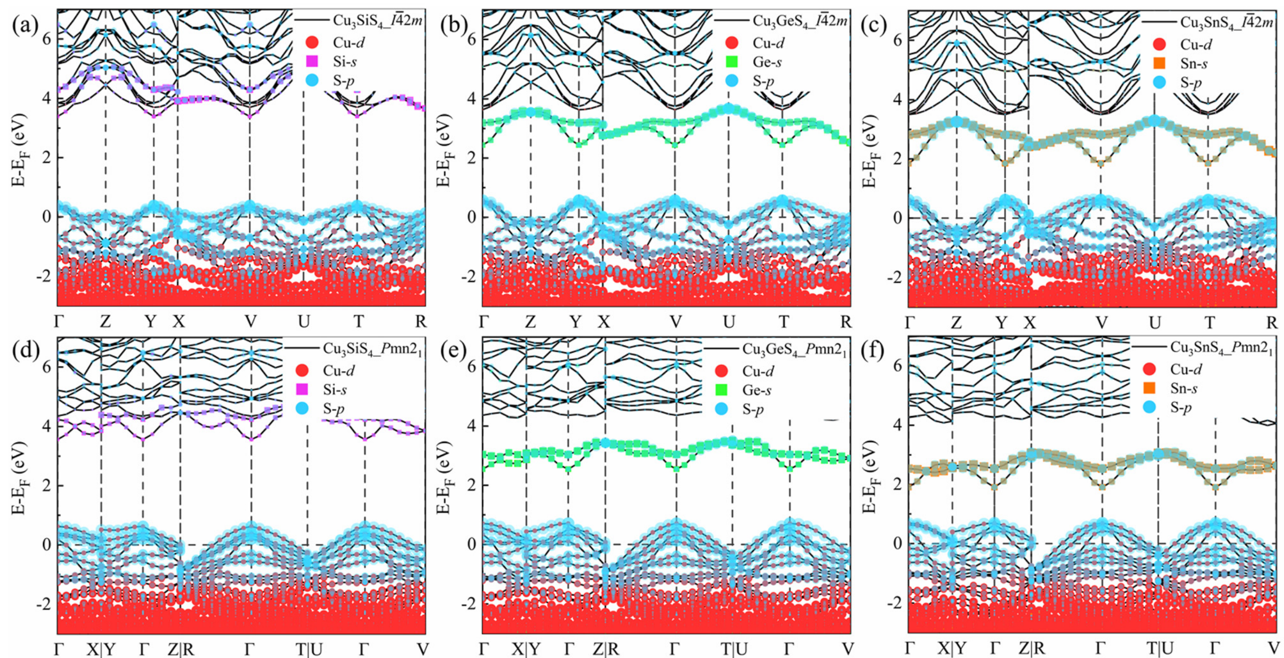

FIG. 2. The calculated fatband plots of Cu_3IVS_4 in tetragonal (a)–(c) and orthorhombic (d)–(f) phases. Red, purple, green, orange, and blue points represent electronic state contributions from Cu-*d*, Si-*s*, Ge-*s*, Sn-*s*, and S-*p* orbitals, respectively. Point size reflects the weight of orbital contribution to the band density of state.

supplementary material) weakens the bonding interaction, which in turn induces a slight downward shift of the CBM and a minor reduction in the E_g. It can be seen that substituting Sn with Ge and Si elements can gradually widen the E_g above the E_F, and the E_g widening effect is particularly pronounced after Si substitution, which has basically met the requirement for visible light transmission. Therefore, Cu_3SiS_4 not only possesses the widest E_g^{tra} but also forms a hole transport channel near the E_F. Additionally, its intra-band absorption (E_g^{int}) occurs below a photon energy of 0.65 eV (Table SII in the supplementary material), making it a promising candidate for high-performance intrinsic *p*-type TCMs.

Building on the aforementioned performance advantages, we will next conduct in-depth studies on the optical properties and structural stability of the lowest-energy orthorhombic Cu_3SiS_4, aiming to clarify its prospects for experimental development as an intrinsic *p*-type TCM. As shown in Fig. 3(a), within the visible light spectrum (380–780 nm), the optical absorption coefficient of orthorhombic Cu_3SiS_4 remains consistently low, all below $2 \times 10^4\ cm^{-1}$. Furthermore, we also evaluated the optical anisotropy; however, the anisotropic behavior is negligible within the visible light region, with discernible differences appearing only in the longer wavelength range (Fig. S5). This absorption directly reflects the material's response to photon energy, where a low absorption coefficient implies photons are less likely to be absorbed, thereby reducing light intensity attenuation while traversing the material. As illustrated in Fig. 3(b), when the material thickness is controlled at approximately 40 nm, its visible light transmittance reaches around 80%. Such optical transparency meets the basic requirements for high-performance TCMs.[31] The high transparency of

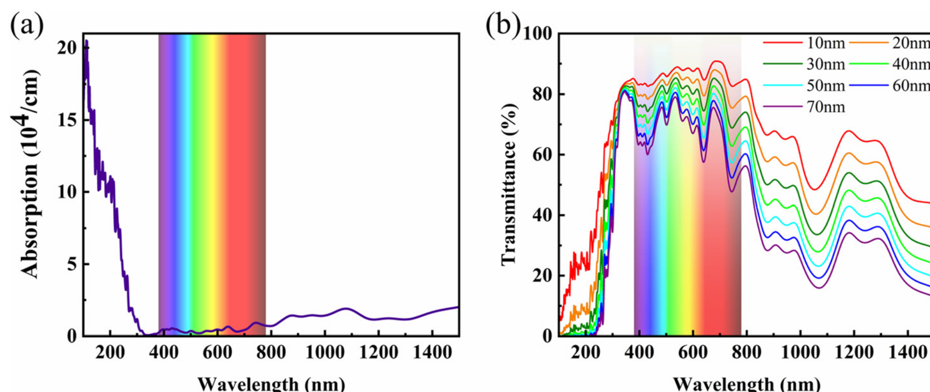

FIG. 3. The calculated absorption coefficient (a) of orthorhombic Cu_3SiS_4 and optical transmittance spectra (b) of orthorhombic Cu_3SiS_4 films with different thicknesses.

05 April 2026 16:11:57

Published under an exclusive license by AIP Publishing

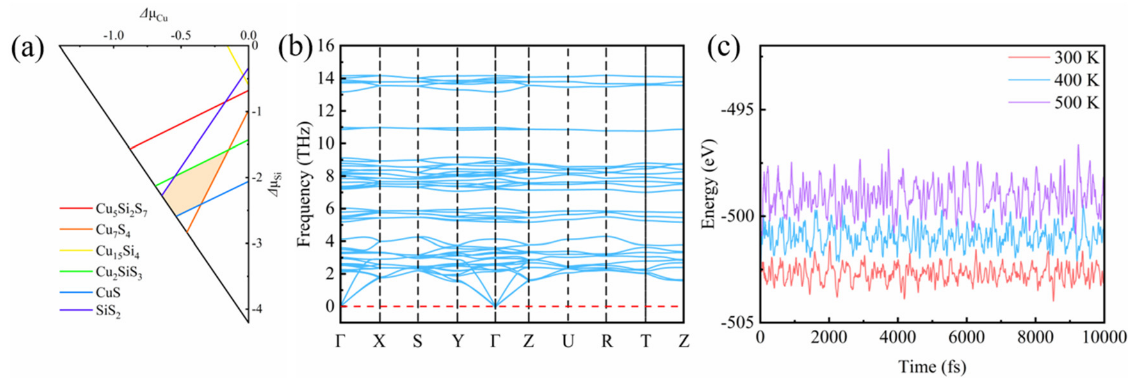

FIG. 4. (a) The allowable ranges (light yellow area) on the relative chemical potential of each element for a stable orthorhombic Cu_3SiS_4 with respect to other competing compounds. (b) The calculated phonon-dispersion spectra of orthorhombic Cu_3SiS_4. (c) Total energies of orthorhombic Cu_3SiS_4 as a function of time during the AIMD simulation at 300, 400, and 500 K.

orthorhombic Cu_3SiS_4 is mainly attributed to the wide E_g^{tra} associated with its unique band structure: the wide energy gap between the E_F and the CBM effectively suppresses the visible light absorption corresponding to interband transitions. Further calculations of the plasma frequency using the Drude formula $\omega_p = \sqrt{\frac{ne^2}{\epsilon_0 m_e}}$ (where n is the free carrier density, e is the electronic charge, ϵ_0 is the static dielectric constant, and m_e is the effective carrier mass) show that under the assumption of one carrier generated per unit cell, its plasma frequency is 3.12 eV/$\hbar$, which is significantly lower than that of metallic aluminum ($\sim$15 eV/$\hbar$).[16] This characteristic results in free carriers being unable to follow the optical field oscillation when the incident light frequency exceeds the plasma frequency, thereby suppressing light reflection and enhancing light transmittance.

To evaluate the thermodynamic stability of the ground state of orthorhombic Cu_3SiS_4, it is necessary to determine whether it decomposes into all possible elemental solids, binary, or ternary compounds.[32] The stability of Cu_3SiS_4 as the host phase requires that the chemical potentials satisfy the equation: $3\Delta\mu_{Cu} + \Delta\mu_{Si} + 4\Delta\mu_S = \Delta H(Cu_3SiS_4) = -4.21$ eV, with the additional constraint that $\Delta\mu_\alpha < 0$ for $\alpha =$ Cu, Si, and S to prevent elemental segregation. For all competing phases, such as $Cu_5Si_2S_7$, Cu_8SiS_6, Cu_2SiS_3, Cu_7S_4, $Cu_{15}Si_4$, CuS, Cu_2S, CuS_2, Cu_9S_5, SiS_2, and SiS_4, the inequality $x\Delta\mu_{Cu} + y\Delta\mu_{Si} + z\Delta\mu_S < \Delta H(Cu_xSi_yS_z)$ must hold, thereby inhibiting their formation and ensuring Cu_3SiS_4 remains the sole stable phase. After accounting for all possible competing elements, binary, and ternary compounds, there exists an allowed range of relative chemical potentials [see the pale-yellow area in Fig. 4(a)]. The presence of this stable region demonstrates that all decomposition reactions of Cu_3SiS_4 are endothermic. Consequently, Cu_3SiS_4 does not decompose spontaneously into other substances and qualifies as a compound with thermodynamic stability. To investigate the stability of Cu_3SiS_4 from the perspective of lattice dynamics, we also performed phonon dispersion spectrum calculations for this compound. The results, presented in Fig. 4(b), reveal an extremely weak imaginary frequency signal (-0.003 eV) near the Γ point of the Brillouin zone. This value is close to the calculation error threshold and can be attributed to the numerical discretization effect caused by the size limitation of the supercell.[33,34] Such a magnitude of imaginary frequency perturbation does not exert a substantial impact on the overall lattice vibration modes of the material, indicating that Cu_3SiS_4 possesses a dynamical stability within the harmonic approximation. To verify the dynamical stability of this structure at finite temperatures, we performed *ab initio* molecular dynamics (AIMD) simulations. Trajectory sampling was conducted for a duration of 10 ps with a time step of 1 fs within the temperature range of 300–500 K [Fig. 4(c)]. The results demonstrate that the total energy of the system fluctuates slightly around the equilibrium value, and no symmetry breaking or atomic dislocation occurs in the crystal structure. Furthermore, extended simulations up to 800 K indicate that the structure remains stable up to 700 K, with decomposition occurring at 800 K (Fig. S4). Collectively, these results confirm that orthorhombic Cu_3SiS_4 exhibits dynamical stability against thermal perturbations over a broad temperature range, laying a theoretical foundation for its experimental preparation.

In summary, this study reveals that orthorhombic Cu_3SiS_4 is a stable, dopant-free p-type transparent conductor through first-principles calculations. The VBM of Cu_3SiS_4 is composed of the antibonding states of Cu-d and S-p, and its E_F can penetrate into the valence band by 0.65 eV, ensuring the p-type electrical conductivity of the material. Meanwhile, the CBM originates from the antibonding states of Si-s and S-p; the stronger bonding interaction between Si-s and S-p can push the CBM upward compared with that formed by the antibonding states of Sn-s and S-p, thereby widening the E_g. The wide E_g^{tra} suppresses visible light absorption induced by interband transitions, enabling the material to maintain high transmittance in the visible light range. Favorable formation energies and stable phonon spectra complete the picture, confirming Cu_3SiS_4 as a robust intrinsic p-type TCM.

See the supplementary material for the Cu_3IVS_4 (IV = Si, Ge, and Sn) crystal structures, the HSE06-calculated PDOS and COOPs, the total energy during AIMD simulations, and the anisotropic absorption coefficients (Figs. S1–S5); the bond lengths of Cu–S/IV–S and the E_g^{int} and E_g widths for different phases (Tables SI and SII); and the computational details of this work.

This work was financially supported by the Natural Science Foundation of Guangxi Province (Grant No. ZY23055002), the

05 April 2026 16:11:57

Published under an exclusive license by AIP Publishing

Guangxi Science and Technology Base and Talent Special Project: Research and Application of Key Technologies for Precise Navigation (Gui Ke No. AD25069103), the Natural Science Foundation of Guangxi Province (Grant No. 2025GXNSFAA069368), and the National Natural Science Foundation of China (Grant No. 61964002). We acknowledge the National High-Performance Computing Center Nanning Branch, the Multifunctional Computer Center of Guangxi University, and the National Academic Infrastructure for Supercomputing in Sweden for providing access to supercomputer resources.

AUTHOR DECLARATIONS

Conflict of Interest

The authors have no conflicts to disclose.

Author Contributions

Changqing Lin: Data curation (equal); Formal analysis (equal); Investigation (equal); Software (equal); Validation (equal); Visualization (equal); Writing – original draft (equal). **Yu-Jun Zhao:** Formal analysis (equal); Investigation (equal); Supervision (equal); Writing – review & editing (equal). **Clas Persson:** Formal analysis (equal); Investigation (equal); Supervision (equal); Writing – review & editing (equal). **Dan Huang:** Conceptualization (lead); Funding acquisition (equal); Project administration (equal); Supervision (equal); Writing – original draft (equal); Writing – review & editing (equal).

DATA AVAILABILITY

The data that support the findings of this study are available from the corresponding author upon reasonable request.

REFERENCES

[1] D. Won, J. Bang, S. H. Choi, K. R. Pyun, S. Jeong, Y. Lee, and S. H. Ko, "Transparent electronics for wearable electronics application," Chem. Rev. **123**(16), 9982–10078 (2023).

[2] K. Ellmer, "Past achievements and future challenges in the development of optically transparent electrodes," Nat. Photonics **6**(12), 809–817 (2012).

[3] X. Cai and S.-H. Wei, "Perspective on the band structure engineering and doping control of transparent conducting materials," Appl. Phys. Lett. **119**(7), 070502 (2021).

[4] A. Stadler, "Transparent conducting oxides—An up-to-date overview," Materials **5**(4), 661–683 (2012).

[5] T. Minami, "Transparent conducting oxide semiconductors for transparent electrodes," Semicond. Sci. Technol. **20**(4), S35–S44 (2005).

[6] X. Jiang, F. L. Wong, M. K. Fung, and S. T. Lee, "Aluminum-doped zinc oxide films as transparent conductive electrode for organic light-emitting devices," Appl. Phys. Lett. **83**(9), 1875–1877 (2003).

[7] A. E. Rakhshani, Y. Makdisi, and H. A. Ramazaniyan, "Electronic and optical properties of fluorine-doped tin oxide films," J. Appl. Phys. **83**(2), 1049–1057 (1998).

[8] S. Calnan and A. N. Tiwari, "High mobility transparent conducting oxides for thin film solar cells," Thin Solid Films **518**(7), 1839–1849 (2010).

[9] D. Huang, Y.-J. Zhao, R.-Y. Tian, D.-H. Chen, J.-J. Nie, X.-H. Cai, and C.-M. Yao, "First-principles study of be doped $CuAlS_2$ for p-type transparent conductive materials," J. Appl. Phys. **109**(11), 113714 (2011).

[10] J. Lee, S. Lee, G. Li, M. A. Petruska, D. C. Paine, and S. Sun, "A facile solution-phase approach to transparent and conducting ITO nanocrystal assemblies," J. Am. Chem. Soc. **134**(32), 13410–13414 (2012).

[11] Z. Chen, W. Li, R. Li, Y. Zhang, G. Xu, and H. Cheng, "Fabrication of highly transparent and conductive indium–tin oxide thin films with a high figure of merit via solution processing," Langmuir **29**(45), 13836–13842 (2013).

[12] M. Ahmadi, M. Asemi, and M. Ghanaatshoar, "Mg and N co-doped $CuCrO_2$: A record breaking p-type TCO," Appl. Phys. Lett. **113**(24), 242101 (2018).

[13] R. Cao, H.-X. Deng, and J.-W. Luo, "Design principles of p-type transparent conductive materials," ACS Appl. Mater. Interfaces **11**(28), 24837–24849 (2019).

[14] Z. Xiao, C. Qiu, S.-H. Wei, and H. Hosono, "Is p-type doping in TeO_2 feasible?," Chin. Phys. Lett. **42**(1), 016103 (2025).

[15] J. Guo and Z. Xiao, "P-type ultrawide E_g spinel $ZnGa_2O_4$: A critical theoretical reevaluation," Phys. Rev. B **112**(19), 195203 (2025).

[16] X. Zhang, L. Zhang, J. D. Perkins, and A. Zunger, "Intrinsic transparent conductors without doping," Phys. Rev. Lett. **115**(17), 176602 (2015).

[17] O. I. Malyi, M. T. Yeung, K. R. Poeppelmeier, C. Persson, and A. Zunger, "Spontaneous non-stoichiometry and ordering in degenerate but gapped transparent conductors," Matter **1**(1), 280–294 (2019).

[18] G. Wang, Y. N. Du, P. Huang, Z. F. Qian, P. Zhang, and S.-H. Wei, "Design of intrinsic transparent conductors from a synergetic effect of symmetry and spatial-distribution forbidden transitions," Phys. Rev. Lett. **134**(3), 036401 (2025).

[19] V. Pavan Kumar, P. Lemoine, V. Carnevali, G. Guélou, O. I. Lebedev, P. Boullay, B. Raveau, R. Al Rahal Al Orabi, M. Fornari, C. Prestipino, D. Menut, C. Candolfi, B. Malaman, J. Juraszek, and E. Guilmeau, "Ordered sphalerite derivative $Cu_5Sn_2S_7$: A degenerate semiconductor with high carrier mobility in the Cu–Sn–S diagram," J. Mater. Chem. A **9**(17), 10812–10826 (2021).

[20] S. He, Y. Luo, L. Xu, Y. Wang, Z. Han, X. Li, and J. Cui, "Remarkable improvement of thermoelectric performance in Ga and Te cointroduced Cu_3SnS_4," Inorg. Chem. **60**(15), 11120–11128 (2021).

[21] Z. Hussain, N. Padha, and A. Banotra, "Development of nanostructured Cu_3SnS_4 thin films through annealing of the stack of precursors for photonic applications," Opt. Quantum Electron. **56**(12), 1976 (2024).

[22] V. R. Minnam Reddy, M. R. Pallavolu, P. R. Guddeti, S. Gedi, K. K. Yarragudi Bathal Reddy, B. Pejjai, W. K. Kim, T. R. R. Kotte, and C. Park, "Review on Cu_2SnS_3, Cu_3SnS_4, and Cu_4SnS_4 thin films and their photovoltaic performance," J. Ind. Eng. Chem. **76**, 39–74 (2019).

[23] P. Arnou, C. S. Cooper, S. Uličná, A. Abbas, A. Eeles, L. D. Wright, A. V. Malkov, J. M. Walls, and J. W. Bowers, "Solution processing of $CuIn(S,Se)_2$ and $Cu(In,Ga)(S,Se)_2$ thin film solar cells using metal chalcogenide precursors," Thin Solid Films **633**, 76–80 (2017).

[24] F. H. Isikgor, S. Zhumagali, L. V. T. Merino, M. De Bastiani, I. McCulloch, and S. De Wolf, "Molecular engineering of contact interfaces for high-performance perovskite solar cells," Nat. Rev. Mater. **8**(2), 89–108 (2022).

[25] Atomly, see https://atomly.matchat.cn/#/matdata for the first principle calculation results on Cu_3SiS_4 and Cu_3GeS_4.

[26] J. E. Saal, S. Kirklin, M. Aykol, B. Meredig, and C. Wolverton, "Materials design and discovery with high-throughput density functional theory: The open quantum materials database (OQMD)," JOM **65**(11), 1501–1509 (2013).

[27] A. J. Cohen, P. Mori-Sánchez, and W. Yang, "Challenges for density functional theory," Chem. Rev. **112**(1), 289–320 (2012).

[28] R. D. Shannon and C. T. Prewitt, "Effective ionic radii and crystal chemistry," J. Inorg. Nucl. Chem. **32**(5), 1427–1441 (1970).

[29] R. D. Shannon, "Revised effective ionic radii and systematic studies of interatomic distances in halides and chalcogenides," Acta Crystallogr., Sect. A **32**(5), 751–767 (1976).

[30] L. Pauling, "The sizes of ions and the structure of ionic crystals," J. Am. Chem. Soc. **49**(3), 765–790 (1927).

[31] G. Brunin, F. Ricci, V.-A. Ha, G.-M. Rignanese, and G. Hautier, "Transparent conducting materials discovery using high-throughput computing," npj Comput. Mater. **5**(1), 63 (2019).

[32] V. Stevanović, S. Lany, X. Zhang, and A. Zunger, "Correcting density functional theory for accurate predictions of compound enthalpies of formation: Fitted elemental-phase reference energies," Phys. Rev. B **85**(11), 115104 (2012).

[33] M. Debbichi and F. Alresheedi, "First-principles calculations of mechanical, electronic and optical properties of a new imidooxonitridophosphate," Chem. Phys. **538**, 110917 (2020).

[34] M. D. Santia, N. Tandon, and J. D. Albrecht, "Effects of strain on the optical and thermodynamic properties of β-Ga_2O_3," Solid State Commun. **297**, 1–5 (2019).

05 April 2026 16:11:57

Published under an exclusive license by AIP Publishing